Point Spread Function Formation in Plane-Wave Imaging: A Theoretical Approximation in Fourier Migration

Chuan Chen[ID], *Student Member, IEEE*, Hendrik H. G. Hansen[ID], *Member, IEEE*,
Gijs A. G. M. Hendriks[ID], *Student Member, IEEE*, Jan Menssen, Jian-Yu Lu[ID], *Fellow, IEEE*,
and Chris L. de Korte[ID], *Senior Member, IEEE*

Abstract—**The point spread function (PSF) is often analyzed to determine the image quality of an ultrasound system. The formation of PSF is determined by practical factors, such as transducer aperture, element directivity, apodization, pitch, imaging position, and steering angle. Conventional numerical simulations provide an iterative approach to examine those factors' effects but cannot explain the inherent mechanism of PSF formation. This article presents a theoretical approximation of PSF formation for plane-wave imaging throughout the Fourier-based reconstruction process. Aforementioned factors are incorporated in the theory. The proposed theory is used to analyze the effects of those factors and presents a high degree of consistency with numerical simulations and experiments.**

Index Terms—**Fourier migration, plane wave, point spread function (PSF).**

I. INTRODUCTION

WITH the progress of ultrafast ultrasound, imaging at kilohertz frame rate has enabled new advanced ultrasound imaging modes, such as shear-wave elastography [1] and ultrafast blood flow mapping [2], as supplements to conventional B-mode and Doppler ultrasound. Instead of focusing ultrasound beams in conventional imaging, ultrafast ultrasound is realized by transmitting one or a few unfocussed ultrasound beams, for example plane waves [3], for large-view insonification. The benefit of high frame rate is compromised by the degradation of image quality due to the absence of focusing in transmission. Although the image quality degradation can be mitigated by coherent compounding [4], the improvement

of image quality remains a significant concern when adopting ultrafast ultrasound imaging.

To assess the image quality of an ultrasound system, the point spread function (PSF) is often determined, representing the ultrasound system's spatial impulse response [5]. The PSF is a combined result of transmit and receive parameters and propagation of acoustic waves. Spatial resolution is usually defined as the full-width at half-maximum of the PSF along lateral, axial, or elevational direction. Apart from the spatial resolution, off-axis sidelobes or grating lobes of the PSF also affect the image contrast [6].

Moreover, PSF plays a central role in restoration methods. Ideally, an ultrasound image can be regarded as the convolution between the PSF and an object function [7]. Therefore, the initial object function can be enhanced by restoring the image using the PSF [8], [9] to obtain an image of much higher resolution. However, in practice, this approach is often difficult to apply successfully, because the mechanism of PSF formation is complicated, that is known to be influenced by multiple factors, such as the position of imaging point, transducer characteristics, beam steering angle, apodization, variation of speed of sound, phase aberration, and reverberation [10]. Specific image beamforming and reconstruction methods also have major influences on the PSF formation [11], [12].

The influences of above factors on the PSF's formation are often examined using numerical ultrasound simulations by software packages such as Field II [13] that models the ultrasound system based on impulse responses [14]. In Field II, the PSF can be estimated by defining a single scattering point as the media object. Although computational simulation can be used to study the PSF, it does not encompass the image formation process. Thus, the inherent mechanism of image reconstruction cannot be fully understood from only the numerical simulation. As an alternative to the computational simulation, a precise theoretical approximation of PSF's formation would be (in principle) more efficient and can illuminate the mechanism of image reconstruction. Revealed mechanism of image reconstruction might set a path for the development of improved image reconstruction methods. In previous studies, Fraunhofer approximation [15] is commonly used to estimate the lateral PSF pattern at the focused point, where waves emitted by the aperture are synchronized [16]. However, the Fraunhofer approximation

can only provide limited insights without disclosing PSF's axial pattern and the effects of steering transmitting angle and off-axis displacement.

In recent years, image reconstruction of ultrafast ultrasound through the Fourier migration has gained attention [17]–[19] as an alternative for the routinely applied delay-and-sum (DAS) beamforming that operates in the temporal domain. Image reconstruction method based on Fourier migration possesses a convincing advantage of higher computational efficiency while producing similar image quality [20]. With respect to plane-wave ultrasound, several studies have explored and refined the reconstruction of plane-wave ultrasound images by using Fourier-based methods [21]–[26]. However, those studies mainly focus on deriving spectrum remapping relations without an in-depth consideration of the aforementioned factors. For example, the finite transducer aperture diameter leads to the PSF's dependence on spatial position. Element directivity and apodization mainly shape the lateral profile of the PSF. The effect of spectrum aliasing related to the element pitch is still in lack of full understanding. By taking these factors into account, Fourier-based image reconstruction can be further improved possibly.

For conventional DAS beamforming, Alberti *et al.* [27] conducted a mathematical analysis of plane-wave PSF's formation using a simplified model without considering the aperture weighting caused by apodization and element directivity. Roquette *et al.* [28] also provided a general expression of the PSF to present the spatially varying feature that can be analyzed through numerical computation. Different from the numerical computation, an analytical expression containing various transducer characteristics and beamforming parameters can provide more valuable insights about the inherent mechanism of PSF formation. With respect to Fourier-based beamforming, there is currently no such analytical expression. Therefore, it is of great importance to derive a comprehensive theory to understand the process of PSF formation in Fourier migration reconstruction.

In this study, we will present a theoretical approximation of PSF's formation throughout the plane-wave image transmission, reception, and spectrum migration process. Aforementioned factors are incorporated into the theoretical model to present a specific PSF and its Fourier spectrum. Validation is conducted by comparing the analytical PSF and spectrum with outcomes from both Field II simulations and experiments.

II. METHODOLOGY

The methodology section is composed of three subsections. In Section II-A, an analytical presentation of the Fourier spectrum of the wavefront from a scattering point is derived through stationary phase approximation. The spectrum of the wavefront can be mapped to the analytical Fourier spectrum of PSF. Section II-B mainly focuses on analyzing the analytical spectrum and the PSF pattern. In Section II-C, simulations and experiments are described, which were used to validate our theory. Variables and symbols used throughout this article are listed in Table I.

TABLE I
LIST OF SYMBOLS AND DESCRIPTIONS

Symbol	Description
x, z, t, c	Lateral and axial coordinates defined by the transducer, time, and sound speed
$\overrightarrow{r_0} = (x_0, z_0)$	Lateral & axial position of scattering point
ϑ, θ	Steering angle of plane wave, the receiving angle with respect to $\overrightarrow{r_0}$: $\theta = \mathrm{atan2}(x_0 - x, z_0)$
$p(x, t, x_0, z_0, \vartheta)$	Signal received by transducer element at $(x, z = 0)$
k_x, k	Lateral wavenumber over $\frac{2\pi}{\Delta x}$ and temporal frequency over $\frac{2\pi}{c\,\Delta t}$,
$P(k_x, k, x_0, z_0, \vartheta)$	Lateral & temporal Fourier transform of received signals $p(x, t, x_0, z_0, \vartheta)$
$k'_x, k'_z, k'_\rho, k'_\varphi$	Spatial wavenumbers of the beamformed image over lateral, axial (orthogonal), angular and radial (polar), respectively
$P(k'_x, k'_z, x_0, z_0, \vartheta),$	Lateral & Axial spectrum after applying the spectrum remapping from $P(k_x, k, x_0, z_0, \vartheta)$
$q(x, z, x_0, z_0, \vartheta)$	Reconstructed RF image by applying inverse Fourier transform of $P(k'_x, k'_z, x_0, z_0, \vartheta)$
$f(x, z)$	Object function
$\Omega(k'_x, k'_z, x_0, z_0, \vartheta)$	The theoretically-derived spectrum weighting function between beamformed spectrum and the object function's spectrum
$\omega(x, z, x_0, z_0, \vartheta)$	Point Spread Function (PSF)
$x \in \left[-\frac{L}{2}, \frac{L}{2}\right]$	The transducer range limited by the aperture size L
μ, D	Element pitch and width
$\varepsilon_k(\theta)$	Element directivity as the function of receiving angle θ that is frequency-dependent
μ_k	Wave attenuation coefficient that is frequency dependent
$\beta_k(\theta, x_0, z_0)$	Wavefront scaling factor contributed by both element directivity, transducer aperture size and wave divergence & attenuation
G	free-space Green's function
$\chi(t)$	The impulse waveform of wavefront
$X(k)$	The temporal Fourier transform of the impulse waveform $x(t)$

A. Analysis of Single Point's Fourier Spectrum

When transducer elements are sequentially excited to uniformly transmit an acoustic impulse $\chi(t)$, a plane wave is generated. By applying linearly increasing time intervals, i.e., time delay, the angle ϑ at which the plane wave travels can be controlled. As shown in Fig. 1, the propagation of this wave in 2-D can ideally be presented as

$$\chi\left(t - \frac{1}{c}(x \sin \vartheta + z \cos \vartheta)\right). \tag{1}$$

As the plane wave propagates across an object, the local variations of the speed of sound and density cause the scattering of waves. These local variations are represented by the function $f(x, z)$. Under the Born approximation (multiple scattering neglected), received signals can be decomposed into independent wavefronts from distributed scattering points.
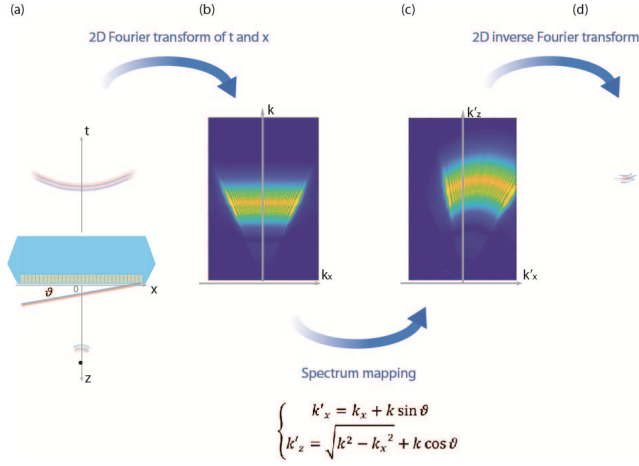
Fig. 1. Schematic of the general Fourier-domain beamforming process, including (a) reception of backscattered wavefront, (b) 2-D Fourier transform to spectrum (k_x, k), (c) spectrum remapping to wavenumber pair (k'_x, k'_z), and (d) reconstructed PSF.

The PSF formation can be analyzed by regarding a single scattering point as the object function. If this point is located at $\vec{r}_0 = (x_0, z_0 > 0)$ to scatter an incident plane wave's energy of one unit, the object function is represented as $f(x, z) = \delta(x - x_0, z - z_0)$. The signal received by a transducer element at $\vec{r} = (x, 0)$ is given by $p(x, t, x_0, z_0, \vartheta)$. As scattered waves travel to the element to generate signals, the transfer function of signal's distant reception can be modeled by free-space Green's function $G(\vec{r}, \vec{r}_0, k) = (e^{-ik|\vec{r}-\vec{r}_0|} / 2\pi |\vec{r} - \vec{r}_0|)$. This signal modeling is valid for wave propagation in homogeneous and isotropic mediums. We adopt the angular wavenumber $k = (2\pi/cT)$, where c and T refer to the speed of sound and the oscillation period, respectively. The decaying factor $(1/|\vec{r} - \vec{r}_0|)$ represents the divergence of a spherical wave from the center source of the scattering point. The frequency-dependent attenuation of acoustic waves can also be modeled as an exponential decaying component $e^{-\mu_k(|\vec{r}-\vec{r}_0|+z_0\cos\vartheta+x_0\sin\vartheta)}$. The common technique to compensate the divergence and the attenuation, time-gain compensation (TGC), is not included in our model. In addition, an apodization function $E(x)$ can be arbitrarily assigned to weight signals.

Noticeably, our model is defined in a 2-D plane without considering the elevational dimension. To include this dimension, the complex 3-D diffraction pattern caused by the elevational focusing should be modeled. This can, for instance, be realized by considering a specific element geometry in a similar way as in Field II, instead of using the free space Green function [29], [30]. If not considering the elevational effect, the temporal spectrum of the signal received at the aperture $(x, 0)$ from a single scattering point at (x_0, z_0) can be modeled as

$$p(x, k, x_0, z_0, \vartheta) = \frac{\varepsilon_k(\theta) X(k) E(x)}{2\pi |\vec{r} - \vec{r}_0|} e^{-(\mu_k+ik)(|\vec{r}-\vec{r}_0|+z_0\cos\vartheta+x_0\sin\vartheta)}$$

(2)

where $X(k)$ represents the temporal spectrum of the impulse waveform accounting for both the reception and transmission transfer function. The term $e^{-(\mu_k+ik)(|\vec{r}-\vec{r}_0|+z_0\cos\vartheta+x_0\sin\vartheta)}$ refers to the time delay and the energy decay through the plane-wave transmission and the reception.

The term $\varepsilon_k(\theta)$ denotes the element directivity as the efficiency of converting the mechanical vibration intensity into the integrated electrical voltage toward a certain receiving angle. It is worthwhile to mention that the definition of element directivity is valid in far field, where $|\vec{r} - \vec{r}_0| \gg 4\pi D^2 k$ such single element can be regarded as a point source. If the elements are planar and square with rigid baffle condition, the element directivity can be depicted by $\varepsilon_k(\theta) = (2\sin(kD\sin(\theta)/2)/kD\sin(\theta))$ [31], whereas, in practice, this term is more complex due to the variation in either surface geometry or excitation voltage. In our model, the element directivity of a sequence of identical elements can be represented as a function of the wave receiving angle $\theta = \arctan(x_0 - x/z_0)$, where arctan represents the arctangent function. This term is specified for a certain angular frequency k, since the element sensitivity varies for different frequencies. Moreover, the signal reception is confined to the transducer aperture range $[-(L/2), (L/2)]$, i.e., $\text{rect}(x/L)$. Here, $\text{rect}(x)$ represents a function to assign its value to be 1 only within $[-(1/2), (1/2)]$ and 0 elsewhere. Moreover, the wavefront energy after scattering is assumed to be isotropic with respect to every receiving angle.

For obtaining the temporal–lateral spectrum of the received signal, Fourier transform of the received signal along the transducer's lateral dimension can be applied

$$P(k_x, k, x_0, z_0, \vartheta)$$
$$= \int p(x, k, x_0, z_0, \vartheta) \text{rect}\left(\frac{x}{L}\right) e^{-ik_x x} dx$$
$$= e^{-(\lambda_k+ik)(z_0\cos\vartheta+x_0\sin\vartheta)}$$
$$\times \int \frac{\varepsilon_k(\theta) X(k) E(x)}{2\pi |\vec{r}-\vec{r}_0|} \text{rect}\left(\frac{x}{L}\right) e^{-(\lambda_k+ik)|\vec{r}-\vec{r}_0|} e^{-ik_x x} dx. \quad (3)$$

Here, we present the lateral wavenumber as $k_x = (2\pi/\lambda_x)$. For excluding evanescent waves, it is required to have $|k_x| < k$ such that the dimensional wavenumber will not exceed the integrated wavenumber.

The estimation of this integral is presented in the Appendix based on the stationary phase approximation method [32]. The stationary phase approximation provides an asymptotic approximation of a fast oscillating integral. The integral value yields significantly around the stationary point, where the derivative and the second-order derivative of phase profile are zero and nonzero, respectively. This approximation requires both the second-order differentiability of phase profile and the continuity of intensity profile. Apart from the stationary point, limits of integral also contribute to the integral value due to the profile discontinuity. According to [33], contributions from the stationary point and the limits of integral are in the order of $O(\lambda^{-1/2})$ and $O(\lambda^{-1})$, respectively, where λ represents the oscillating period. The latter term $O(\lambda^{-1})$ can be regarded as the error bound of the approximation if only the contribution of the stationary point is included [34]. In our model, apodization function $E(x)$ and element directivity $\varepsilon_k(\theta)$ are assumed to be smooth [31], [35] to support the stationary phase approximation. However, the profile discontinuity around aperture borders will increase the error bound of this approximation. This is also illustrated by examples presented in the Appendix.

Using the stationary phase approximation, it is derived that the integral can be approximated as

$$
\begin{aligned}
&P(k_x, k, x_0, z_0, \vartheta) \\
&\approx e^{-\mu_k(z_0 \cos \vartheta + x_0 \sin \vartheta)} X(k) \sqrt{\frac{z_0 k^2}{2\pi \left(k^2 - k_x^2\right)^{3/2}}} \\
&\quad \times e^{-i\left(x_0(k_x + k \sin \vartheta) + z_0\left(k \cos \vartheta + \sqrt{k^2 - k_x^2}\right)\right)} \\
&\quad \times \beta_k\left(\arctan\left(-k_x / \sqrt{k^2 - k_x^2}\right), x_0, z_0\right)
\end{aligned}
\tag{4}
$$

where

$$
\begin{aligned}
\beta_k(\theta, x_0, z_0) &= \varepsilon_k(\theta) \frac{\cos \theta}{z_0} e^{-\frac{\mu_k z_0}{\cos \theta}} \\
&\quad \times E(x_0 - z_0 \tan \theta) \mathrm{rect}\left(\frac{x_0 - z_0 \tan \theta}{L}\right).
\end{aligned}
\tag{5}
$$

$\beta_k(\theta, x_0, z_0)$ is defined as a wavefront intensity scaling factor to present the combining effect of element directivity [$\varepsilon_k(\theta)$], receiving apodization ($E(x_0 - z_0 \tan \theta)$), transducer geometry [$\mathrm{rect}(x_0 - z_0 \tan \theta / L)$], wave's divergence ($\cos \theta / z_0$), and attenuation ($e^{-(\mu_k z_0 / \cos \theta)}$).

In addition to the weighting function described in (5), the spectrum expansion is also restrained by $-(1/2\mu) \leq k_x \leq (1/2\mu)$ to represent the Nyquist sampling limit in lateral dimension. Spectrum exceeding this limit is wrapped into lower frequency section such that the aliasing effect appears. To take this effect into account, we accept a thresholding function $\mathrm{rect}(\mu k_x)$ to exclude spectrum out of range.

In (4), it can be noticed that the exponential phase term $e^{-i[x_0(k_x + k \sin \vartheta) + z_0(k \cos \vartheta + \sqrt{k^2 - k_x^2})]}$ contains an identical wavenumber relation as demonstrated by Cheng and Lu [22], Lu [24], and Liu [21]

$$
\begin{aligned}
k_x' &= k_x + k \sin \vartheta, \\
k_z' &= k \cos \vartheta + \sqrt{k^2 - k_x^2}.
\end{aligned}
\tag{6}
$$

Apart from this exponential phase term, the other terms can be combined as a weighting function

$$
\begin{aligned}
&\Omega(k_x, k, x_0, z_0, \vartheta) \\
&= e^{-\mu_k(z_0 \cos \vartheta + x_0 \sin \vartheta)} X(k) \sqrt{\frac{z_0 k^2}{2\pi \left(k^2 - k_x^2\right)^{3/2}}} \\
&\quad \times \beta_k\left(\arctan\left(-k_x / \sqrt{k^2 - k_x^2}\right), x_0, z_0\right) \mathrm{rect}(\mu k_x)
\end{aligned}
\tag{7}
$$

where $e^{-\mu_k(z_0 \cos \vartheta + x_0 \sin \vartheta)}$ refers to the energy attenuation in transmission process, $X(k)$ represents the Fourier spectrum of impulse waveform, and $\sqrt{(z_0 k^2 / 2\pi (k^2 - k_x^2)^{3/2})}$ is contributed by the wavefront curvature that a flatter wavefront produces a higher value. The function is also weighted by the term of $\beta_k(\arctan(-k_x / \sqrt{k^2 - k_x^2}), x_0, z_0)$, in which element directivity, transducer geometry, wave divergence, and attenuation are incorporated. $\mathrm{rect}(k_x \mu)$ refers to the lateral spectrum range imposed by element pitch.

B. Analysis of PSF's Formation in Fourier Migration

The phase exponential term derived in (6) results in the same wavenumber relation in the f-k beamforming method as derived by Lu [25]. This relation is widely accepted for plane-wave Fourier migration reconstruction. The schematic of described spectrum transform is shown in Fig. 1. In this example, one point source is used to illustrate the transforming process from wavefront to PSF.

If this relation is applied, $P(k_x, k, x_0, z_0, \vartheta)$ can be presented as the function of k_x' and k_z' to be denoted as

$$
P(k_x', k_z', x_0, z_0, \vartheta) \approx \Omega(k_x', k_z', x_0, z_0, \vartheta) e^{-i(x_0 k_x' + z_0 k_z')}
\tag{8}
$$

where the weighting function of k_x' and k_z' is

$$
\begin{aligned}
&\Omega(k_x', k_z', x_0, z_0, \vartheta) \\
&= e^{-\mu_k(z_0 \cos \vartheta + x_0 \sin \vartheta)} X\left(\frac{k_x'^2 + k_z'^2}{2(k_z' \cos \vartheta + k_x' \sin \vartheta)}\right) \\
&\quad \times \beta_k\left(\arctan\left(\frac{\sin \vartheta \left(k_z'^2 - k_x'^2\right) - 2 \cos \vartheta k_x' k_z'}{\cos \vartheta \left(k_z'^2 - k_x'^2\right) + 2 \sin \vartheta k_x' k_z'}\right), x_0, z_0\right) \\
&\quad \times \sqrt{\frac{z_0 (k_z' \cos \vartheta + k_x' \sin \vartheta)(k_x'^2 + k_z'^2)^2}{\pi \left(\cos \vartheta \left(k_z'^2 - k_x'^2\right) + 2 \sin \vartheta k_x' k_z'\right)^3}} \\
&\quad \times \mathrm{rect}\left(\mu \left(\frac{k_x'}{2} + \frac{k_z'}{2} \frac{k_x' \cos \vartheta - k_z' \sin \vartheta}{k_z' \cos \vartheta + k_x' \sin \vartheta}\right)\right).
\end{aligned}
\tag{9}
$$

The interpretation of the weighting function becomes easier when the wavenumbers are transferred into polar coordinates

$$
\begin{aligned}
k_\varphi' &= \arctan\left(\frac{k_x'}{k_z'}\right) \\
k_\rho' &= \sqrt{k_x'^2 + k_z'^2}.
\end{aligned}
\tag{10}
$$

By substituting (6) and (10) into above, the limit of $|k_x| < k$ can be converted to the limit of angle

$$
-\frac{\pi}{4} + \frac{\vartheta}{2} < k_\varphi' < \frac{\pi}{4} + \frac{\vartheta}{2}.
\tag{11}
$$

Within the polar coordinate, $\Omega(k_x', k_z', x_0, z_0, \vartheta)$ can be presented as a function of k_φ' and k_ρ'

$$
\begin{aligned}
&\Omega(k_\varphi', k_\rho', x_0, z_0, \vartheta) \\
&= e^{-\mu_k(z_0 \cos \vartheta + x_0 \sin \vartheta)} \sqrt{\frac{z_0 \cos(k_\varphi' - \vartheta)}{k_\rho'(\cos(2k_\varphi' - \vartheta))^3}} X\left(\frac{k_\rho'}{2 \cos(k_\varphi' - \vartheta)}\right) \\
&\quad \times \beta_k(\vartheta - 2k_\varphi', x_0, z_0) \mathrm{rect}\left(\frac{\mu k_\rho' \sin(2k_\varphi' - \vartheta)}{2 \cos(k_\varphi' - \vartheta)}\right).
\end{aligned}
\tag{12}
$$

It is worthwhile to mention that the limit of wavenumber angle in (11) guarantees the finite value of the weighting template Ω. It can be observed that $\Omega(k_\varphi', k_\rho' x_0, z_0, \vartheta)$ is composed of five parts.

1) The energy attenuation factor in the transmission process: $e^{-\mu_k(z_0 \cos \vartheta + x_0 \sin \vartheta)}$.
2) $X(k_\rho' / 2 \cos(k_\varphi' - \vartheta))$ represents the mapping from impulse waveform spectrum to polar wave vector pair (k_φ', k_ρ'). One may notice that the scale of the spectrum is squeezed by $\cos(k_\varphi' - \vartheta)$ at the angle of k_φ'.
3) $\beta_k(\vartheta - 2k_\varphi', x_0, z_0)$ originates from the wavefront intensity scaling effect that combines element directivity, receiving apodization, transducer geometry, wave's

divergence, and attenuation. It acts as a weighting window in angular dimension shifted by $(\vartheta/2)$. Its narrower distribution produces a smaller angular bandwidth in Fourier domain. As the imaging point moves deeper, the effective receiving angle of β_k is limited to a smaller range, which will lead to a noticeable degradation of the lateral resolution.

4) $\sqrt{(z_0 \cos(k'_\varphi - \vartheta)/k'_\rho (\cos(2k'_\varphi - \vartheta))^3)}$ is the wavefront curvature factor that is depending on imaging depth $(\sqrt{z_0})$, radial wavenumber $(\sqrt{1/k'_\rho})$, and angular wavenumber $(\sqrt{(\cos(k'_\varphi - \vartheta)/\cos(2k'_\varphi - \vartheta))})$. As stated in (11), k'_φ is limited between $-(\pi/4) + (\vartheta/2)$ and $(\pi/4) + (\vartheta/2)$. If k'_φ approaches either margins, this term's value extensively increases but still remains finite. The increase in this term is due to a flatter wavefront at large receiving angle.

5) The threshold function $\text{rect}(\mu k'_\rho \sin(2k'_\varphi - \vartheta)/2\cos(k'_\varphi - \vartheta))$ represents the spectrum range imposed by the element pitch μ. After the spectrum mapping, the simple rectangular function in lateral dimension is tilted by about $-(\vartheta/2)$ for small steering angle ϑ.

Above analysis of the weighting function can be used for PSF estimation. By applying inverse Fourier transform of the remapped spectrum in (8), the PSF at (x_0, z_0) can be reconstructed

$$q(x, z, x_0, z_0, \vartheta)$$
$$= \iint_{-\infty}^{+\infty} P(k'_x, k'_z, x_0, z_0, \vartheta)e^{i(xk'_x + zk'_z)}dk'_x dk'_z$$
$$\approx \iint_{-\infty}^{+\infty} \Omega(k'_x, k'_z, x_0, z_0, \vartheta)e^{-i(x_0 k'_x + z_0 k'_z)}$$
$$\times e^{i(xk'_x + zk'_z)}dk'_x dk'_z. \tag{13}$$

Following the convolution theory, we can obtain the PSF in the convolution form:

$$q(x, z, x_0, z_0, \vartheta)$$
$$\approx \left(\iint_{-\infty}^{+\infty} \Omega(k'_x, k'_z, x_0, z_0, \vartheta)e^{i(xk'_x + zk'_z)}dk'_x dk'_z \right)$$
$$* \left(\iint_{-\infty}^{+\infty} e^{-i(x_0 k'_x + z_0 k'_z)}e^{i(xk'_x + zk'_z)}dk'_x dk'_z \right)$$
$$= \omega(x, z, x_0, z_0, \vartheta) * \delta(x - x_0, z - z_0)$$
$$= \omega(x - x_0, z - z_0, x_0, z_0, \vartheta). \tag{14}$$

Here, $\omega(x, z, x_0, z_0, \vartheta)$ is the PSF, which is the inverse Fourier transform of the weighting function $\Omega(k'_x, k'_z, x_0, z_0, \vartheta)$. Sign $*$ represents the 2-D convolution relation. It can be deduced that the PSF pattern is determined by the weighting function Ω, while the PSF position is controlled by the exponential term.

From the analysis of spectrum weighting in (12), one can observe that the PSF is mainly affected by two components: the impulse waveform spectrum depicted by X mainly in radial dimension and the weighting profile determined by both intensity scaling ratio β_k and the wavefront curvature term in angular dimension.

Moreover, it is worthwhile to mention the influence of the exponential term $e^{-i(x_0 k'_x + z_0 k'_z)}$ on the PSF. In an ideal

	Simulation	Experiment
Elements number	256	128
Element pitch (mm)	0.15	0.197
Element Width (mm)	0.1	0.15
Central Frequency (MHz)	5.0	7.8
Sampling Frequency (MHz)	40	31.3
Excitations (Nr. cycles)	2	4

situation, this term only controls the PSF position. However, potential sound speed variance and phase aberration will undermine this exponential term's accuracy, which results in deformation and spatial shift of the PSF pattern.

C. Validation in Simulation and Experiment

To examine the accuracy of the proposed theory, we conducted both simulations and experiments. Simulated and experimental PSFs were compared to their patterns and Fourier spectra derived from the proposed theory. Transducer parameters in experiments and simulations are listed in Table II. The experiment uses 128 elements with fixed pitch-to-wavelength ratio about 1. In simulation, the pitch-to-wavelength ratio is set to 0.5 to allow broader lateral bandwidth for expanding the spectrum. The simulated transducer employs a larger number of elements to obtain a relatively larger aperture.

Field II software package [34] was used to simulate the process of transmit, scatter, and reception. The simulation computes the impulse responses from scattering points to each element. Simulated RF signals were processed following the spectrum transformation and remapping approaches introduced in Section II. This process is similar to the method proposed by Lu [24], while leaving out a weighting on the Fourier spectrum. Simulations of PSF were repeated for multiple scenarios in which we varied: 1) the position of the scattering point along the depth and lateral directions; 2) the apodization setting in receive; and 3) the plane-wave steering angle.

For experiments, an ATL (ATL, Bothell, WA, USA) linear L12-5 38-mm probe was connected to a Verasonics V1 128-channel ultrasound system (Redmond, WA, USA). Plane-wave data set was acquired by imaging a wire target immersed in water. The diameter of this wire was 0.05 mm, and thus, it can be regarded as a single scattering point in the axial–lateral plane. We used 128 elements in transmission and reception.

For validation, PSFs and their spectra obtained in simulations or experiments are compared with PSFs and spectra estimated in theory. In the comparison, an arc band of the spectrum amplitude and a lateral line of the PSF envelope were extracted and evaluated. An amplitude distribution was calculated at the average spectrum intensity in an arc band of 400 m^{-1} wide along the arc of radius $k'_\rho = (2f_c/c)$. An intensity profile was measured on the line, laterally crossing the peak of the PSF envelope, which was obtained by applying Hilbert transformation. Spectrum amplitude distributions and PSF envelope intensity profiles were aligned by

simply matching their spectrum 0° sections and the profile peaks, respectively. After aligning PSF patterns, mean error was calculated as the intensity difference normalized by the peak value, for the region where the envelope is higher than 0.1% of the peak value. This small threshold includes the central PSF pattern and major sidelobes, while the mean value will not become extremely low in averaging the pattern over a large region.

Theoretical estimation of the analytical spectrum was based on (4) and (9). Using only one scattering point target, the impulse waveform $\chi(t)$ was estimated from the received wavefront recorded on 32 elements that are centered around the lateral position of the point target. We used only 32 elements because these channels have higher signal energies relative to thermal noise. Signals were sequentially extracted, interpolated, aligned, and finally summed up to form the impulse waveform. Contributed by element directivity, wavefront attenuation, and divergence, or target's scattering pattern, the combined analytical intensity scaling ratio $\beta_k(\theta)$ was approximated by fitting a Gaussian function with the measured wavefront intensity distribution. Gaussian function provides a certain flexibility in fitting the coarse intensity distribution that is supposed to be smooth and symmetric. Here, intensity ratio's dependence on frequency was not taken into account.

III. RESULT

A. Effects of Point Depth and Lateral Position

Within the analytical model, the influence of scattering point's position is mainly reflected in β_k. In Fig. 2, beamformed PSFs and their spectra at 5-, 20-, and 40-mm depths are presented for comparison. The mean error between analytical PSF envelope and simulated one is 0.59%, 0.35%, and 0.76%.

For a shallow imaging point at 5 mm as shown in Fig. 2(a), a broad analytical spectrum is bounded within the thresholding template $\text{rect}(x/L)$ to mimic the aliasing effect of wrapping spectrum. Wrapping spectrum produces apparent sinc oscillating artifacts. As the scattering point moves deeper, the angular spectrum becomes more uniform and narrower to be contained within the thresholding template. Thus, significant sinc oscillating lobes caused by wrapping spectrum are no longer present. A narrower angular spectrum produces a smaller angular gap between sidelobes. Because a narrower angular spectrum will broaden the PSF envelope profile, the lateral resolution decreases for deeper imaging point.

For a scattering point positioned at 20-mm depth, spectra and PSFs for lateral shifts of 0, 7.5, and 15 mm are presented in Figs. 2(b) and 3. Mean errors between analytical PSF envelop and simulated envelope are 0.35%, 0.28%, and 0.43%. As expected, PSF pattern and spectrum distribution are horizontal symmetric when the point is in the middle and asymmetric when the point is shifted. It can be observed that the angular spectrum is rotated toward the anticlockwise direction, as the imaging point moves to a positive lateral position. The spectrum change over the point's lateral position is also reflected in anticlockwise tilting PSF patterns.
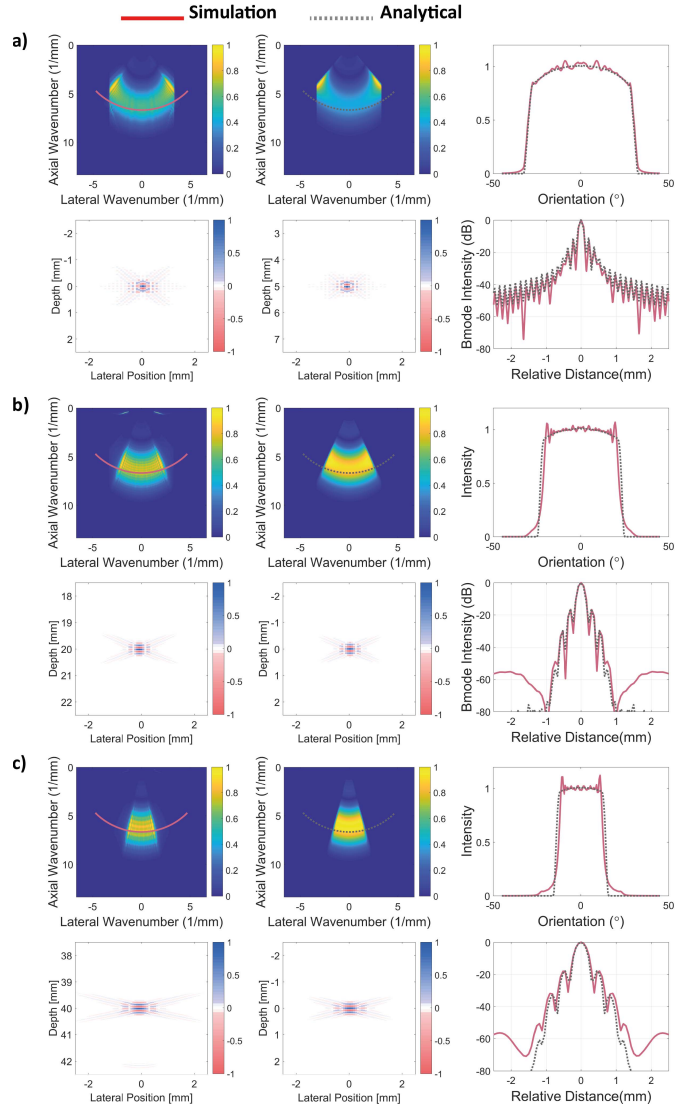

Fig. 2. Effect of imaging point's depth on PSF and spectrum. Along the middle line, imaging point is positioned at (a) 5, (b) 20, and (c) 40 mm deep, respectively. Plane wave is steered at 0° by a 256-element transducer. In each subfigure, the first two columns represent Fourier spectrum (top) and PSF (bottom) in simulation and analytical derivation, respectively. The last column contains spectrum amplitude distribution and PSF lateral envelope intensity profiles compared between simulation (red solid line) and analytical derivation (gray dotted line). Spectrum amplitude distributions are measured along an arc labeled in first two columns. PSF lateral envelope profiles are measured along the horizontal line across the intensity peak. From (a) to (c), errors between analytical PSF envelope profile and simulated one are 0.59%, 0.35%, and 0.76%, respectively.

B. Effect of Receiving Apodization

In our theoretical model, element directivity, transducer geometry, and receiving apodization are combined in the wavefront intensity scaling factor β_k. This factor determines both the lateral profile and the rotation of PSF to a large extent. Fig. 4 presents the results for three different apodization settings: full Hanning, double adjunct Hannings, and half aperture of 64 elements. Mean errors between analytical PSF and simulated envelopes are 0.19%, 0.28%, and 0.32%. The Hanning and the half aperture are similar to straightforward
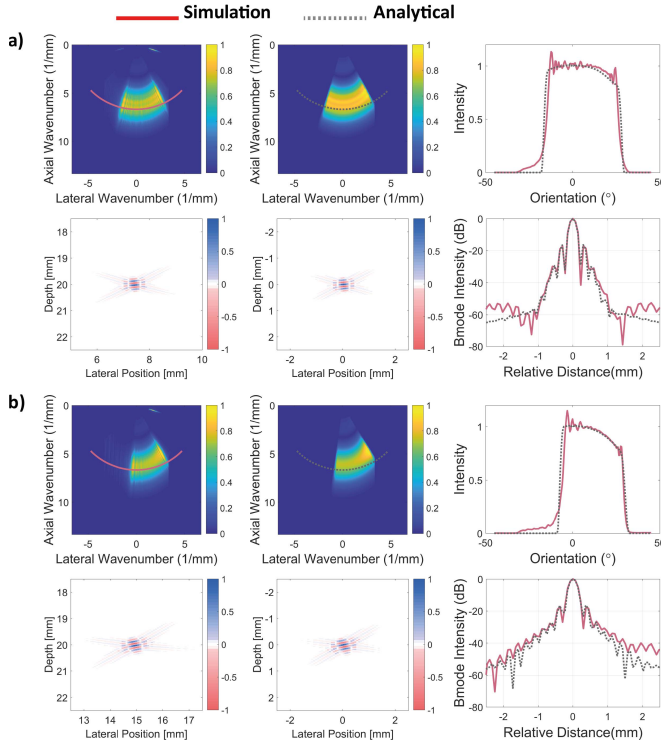
Fig. 3. Effect of imaging point's lateral position on PSF and spectrum. Along the depth of 20 mm, imaging point is laterally shifted for (a) 7.5 and (b) 15 mm. The example at the middle of 20-mm depth is in Fig. 2(b). Plane wave is steered at 0° by a 256-element transducer. Layout and setting of each subfigure are the same as Fig. 2. Errors between analytical PSF envelope profile and simulated one are 0.28% for (a) and 0.43% for (b).

apodizations in DAS with decreased lateral resolution. The double-Hanning function is similar to the transversal oscillation technique [35]. One can have an intuitive observation that the spectrum amplitude distribution is weighted by the apodization function in angular dimension.

The weighting function across the spectrum angular profile is also manifested in the PSF pattern. Hanning window suppresses the sidelobes and smooths the PSF lateral profile at the expense of lateral resolution. This outcome is similar to the observation in designing the apodization of DAS. In the last case of the double-Hanning window, an oscillation pattern of the PSF's lateral profile can be observed similar to transversal oscillation technique.

C. Effect of Plane-Wave Steering Angle

If the plane wave is transmitted toward a certain angle, it can be deduced from (6) that the remapped spectrum will be tilted. For a point positioned at 20-mm depth in the middle, PSFs and spectra produced for 0°, 10°, and 20° plane waves are presented in Figs. 2(b) and 5(a) and (b). We also present an example of shifting the point for 7.5 mm and steering the plane wave at 10°. For these examples, mean errors between analytical PSF and simulated envelopes are 0.35%, 0.38%, and 0.41%. It is shown that spectrum and PSF rotate in the anticlockwise direction when steering plane wave toward larger angles.
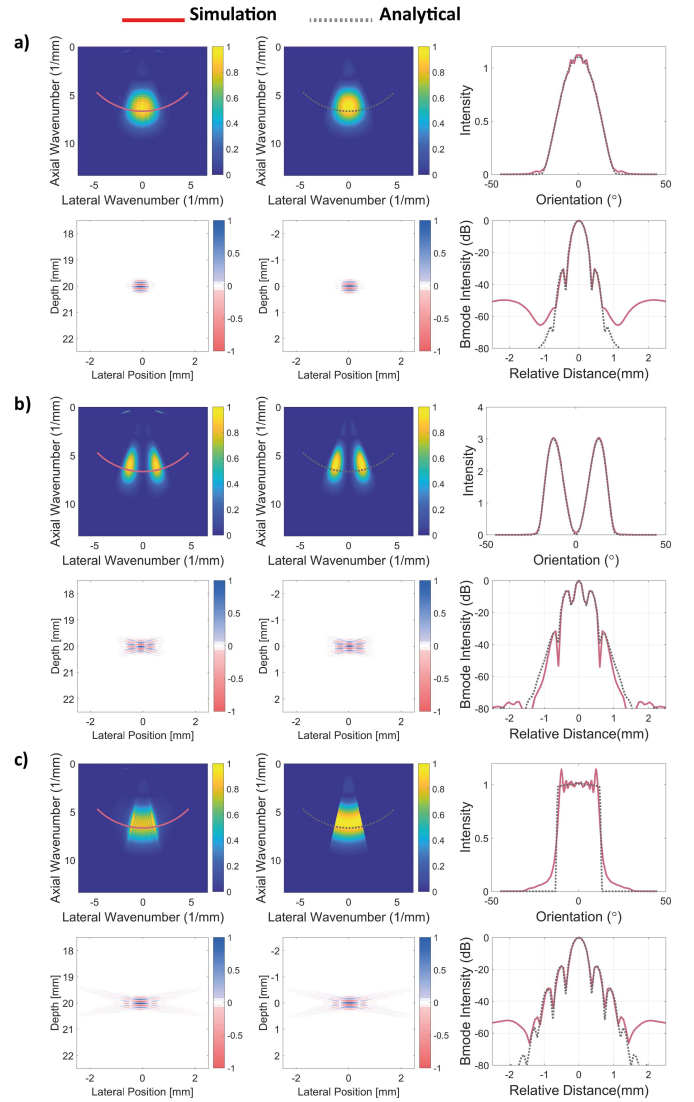

Fig. 4. Effect of receiving apodization on PSF and spectrum. Three apodization windows (a) Hanning, (b) double-Hannings, and (c) half aperture. Plane wave is steered at 0° by a 256-element transducer. Layout and setting of each subfigure are the same as Fig. 2. From (a) to (c), errors between analytical PSF envelope profile and simulated one are 0.19%, 0.28%, and 0.32%, respectively.

D. Validation in Experiment

To further validate the theory, analytical spectra and PSFs are also compared with the experimental results as presented in Fig. 6. In Fig. 6(a) and (b), the wire target is positioned in the middle and around 17-mm depth with plane waves at angles of 0° and 20°. Fig. 6(c) presents a case of shifting wire for 6 mm and steering plane wave at 10°. Mean errors between analytical PSF and simulated envelopes are 0.51%, 0.65%, and 0.49%. Similar to the simulation of plane-wave steering in Fig. 5, one can observe the rotation of spectrum and PSF in both experiment and analytical results.

IV. DISCUSSION

A. Accuracy of Proposed Theory

We present and comprehensively analyze a theoretical model of PSF's formation in Fourier-based beamforming
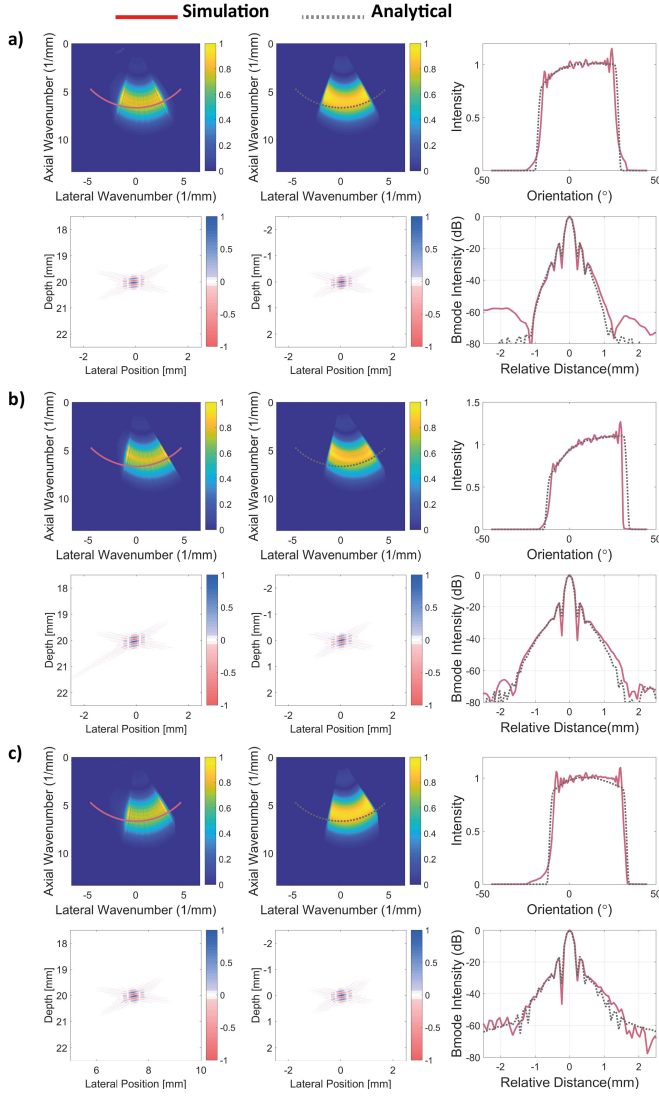
Fig. 5. Effect of plane-wave steering angle on spectrum and PSF. For a point positioned in the middle of 20-mm depth, plane wave is steered toward at (a) 10° and (b) 20°. The image of 0° can be found in Fig. 2(b). (c) Image of steering 10° and lateral shift of 7.5 mm. The transducer contains 256 elements. Layout and setting of each subfigure are the same as Fig. 2. From (a) to (c), errors between analytical PSF envelope profile and simulated one are 0.38%, 0.41%, and 0.38%, respectively.
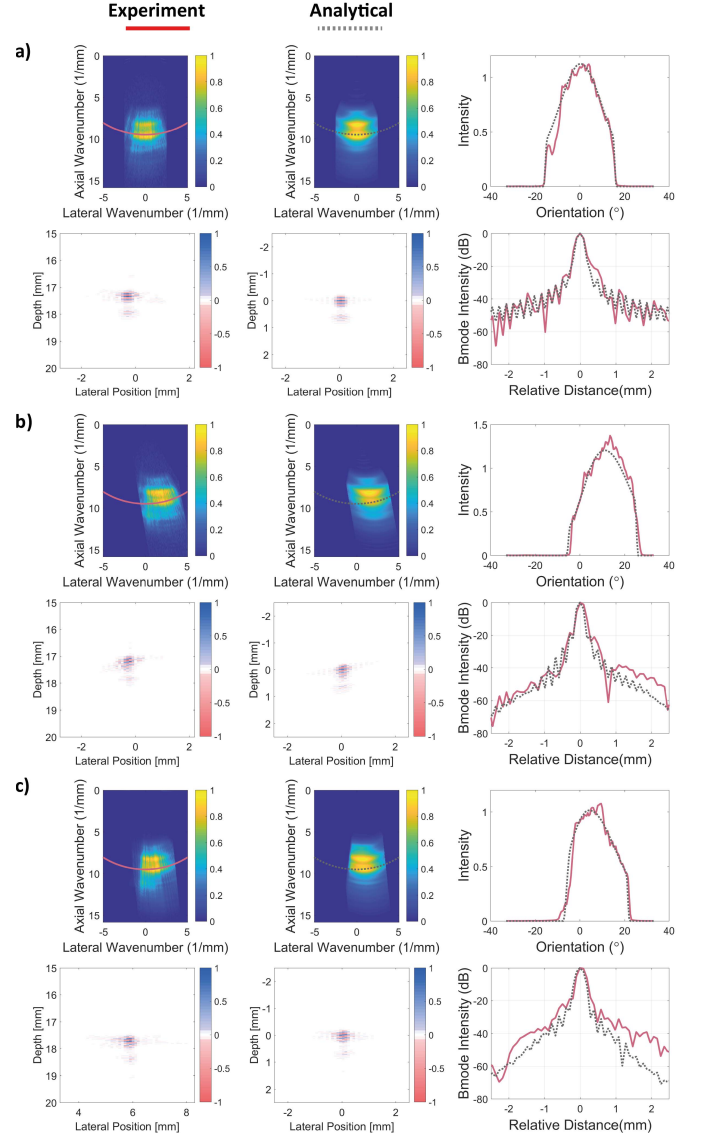

Fig. 6. Validation of spectrum and PSF in experiment. In (a) and (b), L12-5 transmits plane waves at 0° and 20° to insonify a wire located in the middle of 17-mm depth. In (c), the wire is shifted by 6 mm, and the steering angle is 10°. Layout and setting of each subfigure is the same as Fig. 2. From (a) to (c), mean errors between experimental PSF envelope profile and analytical one are 0.51%, 0.65%, and 0.49%, respectively.

process. An analytical expression was carried out to depict the spectrum and PSF. In this expression, multiple factors, including the transducer geometry, plane-wave steering angle, transducer characteristics, and receiving apodization, are taken into account. In comparison with simulations and experiments, the proposed theory shows high accuracy in predicting spectrum distribution and PSF. The lateral aliasing effect is properly approximated by imposing an arbitrary thresholding template, as shown in Figs. 2(a) and 6.

It can be noticed that apparent oscillating patterns appear across the simulated and experimental spectrum amplitude distribution with exceptions of smooth profiles in Fig. 4(a) and (b). This can be explained by Gibbs phenomena that are mainly related to limited aperture diameter in representing a steep spectrum distribution. The mismatch between coarse practical

spectra and smooth analytical ones can be regarded as the stationary phase approximation error induced by discontinuities around aperture borders. Noticeably, the spectrum mismatch is not directly reflected in the quantified PSF envelope error.

For PSF, the theory also shows high accuracy in depicting the simulated or experimental PSF pattern. In line with the transition of spectrum, PSF is shown to be either rotated or reshaped when moving the point position or changing the apodization. These PSF changes were also accurately predicted by our theory. The mean error between simulated PSF and analytical envelopes is mainly within 0.19%–0.51% except for the larger error 0.76% in the 4-cm depth case. The mean error for experimental PSFs is larger to be within
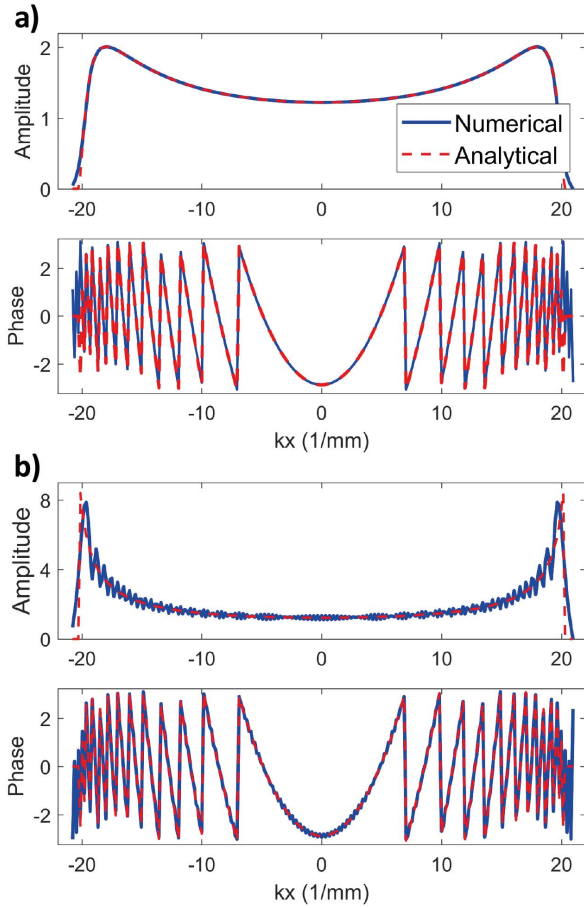
Fig. 7. Comparisons between numerical and analytical integral values for amplitude (top) and phase (bottom), computed for (a) full-aperture Hanning and (b) rectangular apertures.

0.49%–0.65%. This difference can be mainly explained by the coarser wavefront intensity profile in experiment, while the profile in analytical approximation is fitted by a Gaussian function. The increasing error in experiment can also be caused by the aliasing artifact given the larger pitch-to-wavelength ratio.

B. Limitations of Theoretical Model

Although the proposed theoretical model presents high accuracy in depicting the spectrum distribution and PSF shape, there are multiple factors that might limit its accuracy and applicability in practice.

The primary limitation is the error of stationary phase approximation that depends on the second-order differentiability of phase profile and the continuity of intensity profile. Regarding the phase profile, both phase aberration and variation of the speed of sound are potential to undermine the differentiability of phase profile. Regarding the intensity profile, it cannot be modeled as smooth when elements present nonuniform directivities or a nonsmooth apodization is applied. As explained in the method section, the discontinuity around the aperture border serves as the error bound of stationary phase approximation. This effect is shown in the comparison between the smooth and the discontinuous

apodization examples in Fig. 4. Furthermore, the transmission processing is modeled as an ideal plane-wave propagation, while, in practice, sidelobes and grating lobes may also become significant in those cases of low wavelength-to-pitch ratio and large steering angle. This grating lobe has not been considered in the proposed theory.

In addition, different from the direct approximation of the integral in our theoretical approximation, the aliasing effect of discrete Fourier transform (DFT) in practical beamforming is a significant bottleneck due to insufficient sampling. Because the lateral frequency range is limited by the element pitch, the spectrum content beyond the limit will be wrapped inside to cause aliasing artifact. For plane-wave ultrasound, the aliasing will occur on the wavefront section with a steep slope, particularly for the shallow imaging depth. To account for the effect of limited bandwidth, an arbitrary thresholding template is introduced in (7). The effectiveness of such template can be examined in the example of Fig. 2(a), where significant sinc oscillation pattern appears for a point at shallow depth.

Furthermore, our model is based on the Born approximation, which assumes multiple scattering to be at least 50 dB lower than direct scattering. This approximation is challenged in the presence of significant phase aberration caused by reflection, diffraction, and speed of sound variance. Proposed model also neglects the elevational dimension, where the beam profile produced by element geometry influences the field intensity on both transmit and receive. Future work is expected to also incorporate the phase aberration and the elevational dimension into the model.

C. Potential Applications

Notwithstanding aforementioned limitations, our theoretical model provides a guidance on Fourier-based beamforming and postprocessing of plane-wave ultrasound. Given the point's position, transducer characteristics, and beamforming setting, both the spectrum and the PSF can be accurately predicted. In this sense, the theory provides a fast way to determine those effects of transducer settings, beamforming and imaging settings on PSF, and, thus, resolution and sidelobe levels (CNR). This might be useful to determine the feasibility of a specific beamforming method or imaging optimization setting to obtain optimal resolution and CNR for any position within the imaging view. Although the effectiveness of image restoration from PSF using deconvolution is controversial for ultrasound, this work may facilitate the development of a practical restoration technique.

Furthermore, proposed theory based on stationary phase approximation can also be extended to other techniques, such as diverging wave and synthetic aperture imaging. With respect to the diverging wave imaging, it still does not exist as a general wavenumber mapping relation applicable for the entire volume. Using our method, the derivation of the specific relation for a certain region is straightforward. Similarly, the PSF formation in Fourier-based beamforming of synthetic aperture imaging can also be analyzed through our approach by incorporating the transducer characteristics and the imaging position.

V. CONCLUSION

In this study, a theoretical model of PSF's formation is presented for plane-wave Fourier-based beamforming. Multiple factors, such as the transducer geometry, plane-wave steering angle, and point's position, are included in the model. Spectra and PSFs from theoretical approximation are similar to those spectra and PSFs from simulations and experiments. Proposed theoretical model can provide a guidance to optimize the beamforming and postprocessing of plane-wave ultrasound.

APPENDIX
INTEGRAL APPROXIMATION BY THE STATIONARY PHASE METHOD

The integral in (3) can be approximated by the stationary phase method [21]. The integral is

$$
\begin{aligned}
&P(k_x, k, x_0, z_0, \vartheta) \\
&= \int_{-\infty}^{+\infty} p(x, k) \mathrm{rect}\left(\frac{x}{L}\right) e^{-ik_x x} dx \\
&= e^{-(\lambda_k + ik)(z_0 \cos \vartheta + x_0 \sin \vartheta)} \\
&\quad \times \int_{-\infty}^{+\infty} \frac{\varepsilon_k(\theta) X(k) E(x)}{2\pi |\vec{r} - \vec{r}_0|} \mathrm{rect}\left(\frac{x}{L}\right) e^{-(\lambda_k + ik)|\vec{r} - \vec{r}_0|} e^{-ik_x x} dx.
\end{aligned}
$$
(A.1)

Given $\vec{r} = (x, 0)$ and $\vec{r}_0 = (x_0, z_0)$, the Cartesian coordinate can be converted to polar form as $\theta = \arctan(x_0 - x/z_0)$, where arctan represents the arctangent function. Correspondingly, $x = x_0 - z_0 \tan \theta$ and $|\vec{r} - \vec{r}_0|$ is equal to $(z_0/\cos \theta)$. We can use

$$
\begin{aligned}
&\beta_k(\theta, x_0, z_0) \\
&= \varepsilon_k(\theta) \frac{\cos \theta}{z_0} e^{-\frac{\lambda_k z_0}{\cos \theta}} \mathrm{rect}\left(-\frac{z_0}{L} \tan \theta + \frac{x_0}{L}\right) E(x_0 - z_0 \tan \theta)
\end{aligned}
$$
(A.2)

to represent the wavefront intensity scaling factor as a function of receiving angle. This factor combines those effects of element directivity, receiving apodization, wave divergence, attenuation, and transducer geometry. This received wavefront intensity is presented with respect to angle from $\vec{r}_0$ to $\vec{r}$.

Using such a notation, (A.1) can be presented as

$$
\begin{aligned}
&P(k_x, k, x_0, z_0, \vartheta) \\
&= e^{-(\lambda_k + ik)(z_0 \cos \vartheta + x_0 \sin \vartheta)} \frac{X(k)}{2\pi} \\
&\quad \times \int_{-\infty}^{+\infty} \beta_k\left(\arctan\left(\frac{x - x_0}{z_0}\right), x_0, z_0\right) \\
&\quad \times e^{-\left(k_x x + k\sqrt{(x_0 - x)^2 + z_0^2}\right)} dx.
\end{aligned}
$$
(A.3)

To explain the stationary phase approximation, we let $g(x) = \beta_k(\arctan(x - x_0/z_0), x_0, z_0)$ and $f(x) = k_x x + k\sqrt{(x_0 - x)^2 + z_0^2}$. If k mainly consists of high-frequency content (around the central frequency), $f(x)$ is a rapidly varying function. Rapid oscillation of the exponential term means that the integral is approximately zero except the section where $f'(x) = 0$. The point satisfying the zero derivative is labeled as x_s. Expanding $f(x)$ into Taylor series near the point x_s

$$
f(x) \approx f(x_s) + \frac{1}{2} f''(x_s)(x_s - x)^2.
$$
(A.4)

Using the stationary phase approximation, the integral in (A.2) can be approximated as

$$
\begin{aligned}
&\int_{-\infty}^{+\infty} \beta_k\left(\arctan\left(\frac{x - x_0}{z_0}\right), x_0, z_0\right) e^{-i\left(k_x x + k\sqrt{(x_0 - x)^2 + z_0^2}\right)} dx \\
&= \int_{-\infty}^{+\infty} g(x) e^{-if(x)} dx \approx \sqrt{\frac{2\pi}{if''(x_s)}} g(x_s) e^{-if(x_s)}.
\end{aligned}
$$
(A.5)

Given k_x and k, $(\partial f / \partial x) = 0$ is satisfied at point $x_s = x_0 - (k_x / \sqrt{k^2 - k_x^2}) z_0$. Around this point

$$
\begin{aligned}
f(x_s) &= k_x x_0 + z_0 \sqrt{k^2 - k_x^2}, \\
f''(x_s) &= \frac{(k^2 - k_x^2)^{3/2}}{k^2 z_0}.
\end{aligned}
$$
(A.6)

Substituting (A.5) into (A.4), the integral becomes

$$
\begin{aligned}
&\int_{-\infty}^{+\infty} g(x) e^{-if(x)} dx \\
&\approx g(x_s) \sqrt{\frac{2\pi}{if''(x_s)}} e^{-if(x_s)} \\
&= \beta_k\left(\arctan\left(-k_x / \sqrt{k^2 - k_x^2}\right)\right) \\
&\quad \times \sqrt{\frac{2\pi z_0 k^2}{(k^2 - k_x^2)^{3/2}}} e^{-i\left(k_x x_0 + z_0 \sqrt{k^2 - k_x^2}\right)} e^{-i\frac{\pi}{4}}.
\end{aligned}
$$
(A.7)

Considering the spatial shifting property, the influence of the phase term $e^{-i(\pi/4)}$ becomes insignificant for high frequency k. This term will be neglected in the following text. Using the result of the approximation, the integral in (A.2) is approximated as

$$
\begin{aligned}
&P(k_x, k, x_0, z_0, \vartheta) \\
&\approx e^{-\lambda_k(z_0 \cos \vartheta + x_0 \sin \vartheta)} \beta_k\left(\arctan\left(-k_x / \sqrt{k^2 - k_x^2}\right), x_0, z_0\right) \\
&\quad \times X(k) \sqrt{\frac{z_0 k^2}{2\pi (k^2 - k_x^2)^{3/2}}} e^{-i[x_0(k_x + k\sin\vartheta) + z_0(k\cos\vartheta + \sqrt{k^2 - k_x^2})]}.
\end{aligned}
$$
(A.8)

In the above derivation, the approximation requires both the second-order differentiability of the phase profile $f(x)$ as well as the continuity of the intensity profile $g(x) = \beta_k(\arctan(x - x_0/z_0), x_0, z_0)$. Due to the term $\mathrm{rect}(-(z_0/L)\tan\theta + (x_0/L))$, function β_k may become discontinuous around the aperture border, which can lead to an error in the integral calculation [34]. As illustrated in Fig. 7, the error is usually, in case of a smooth apodization function, negligible, but can reach values of ∼10% in highly discontinuous cases. Here, we present two examples to illustrate the error induced by discontinuous aperture borders. Given an array of $N = 256$ elements with a pitch $\Delta x = 150$ μm, a wavenumber $k = (2\pi F_c / c)$ with $F_c = 5$ MHz, and $c = 1540$ m/s, we can calculate the DFT of the wavefront scattered at $(x_0, z_0) = [0, 5]$ mm using (A.8). Resulting amplitude and phase values are presented below for a full-aperture rectangular and a Hanning apodization profile, respectively, representing cases of discontinuous and

continuous aperture borders. For the rectangular profile, mean absolute errors between numerical and analytical solutions are 12.1% and 6.5% for the amplitude and phase. For the Hanning profile, normalized errors are 0.30% and 3.3%. The significantly increased error of the rectangular profile can be attributed to the inaccuracy around the discontinuous aperture border.

REFERENCES

[1] J. Bercoff, M. Tanter, and M. Fink, "Supersonic shear imaging: A new technique for soft tissue elasticity mapping," *IEEE Trans. Ultrason., Ferroelectr., Freq. Control*, vol. 51, no. 4, pp. 396–409, Apr. 2004.

[2] J. Bercoff *et al.*, "Ultrafast compound Doppler imaging: Providing full blood flow characterization," *IEEE Trans. Ultrason., Ferroelectr., Freq. Control*, vol. 58, no. 1, pp. 134–147, Jan. 2011.

[3] M. Tanter and M. Fink, "Ultrafast imaging in biomedical ultrasound," *IEEE Trans. Ultrason., Ferroelectr., Freq. Control*, vol. 61, no. 1, pp. 102–119, Jan. 2014.

[4] G. Montaldo, M. Tanter, J. Bercoff, N. Benech, and M. Fink, "Coherent plane-wave compounding for very high frame rate ultrasonography and transient elastography," *IEEE Trans. Ultrason., Ferroelectr., Freq. Control*, vol. 56, no. 3, pp. 489–506, Mar. 2009.

[5] B. W. Drinkwater and P. D. Wilcox, "Ultrasonic arrays for non-destructive evaluation: A review," *NDT E Int.*, vol. 39, no. 7, pp. 525–541, Oct. 2006.

[6] D. A. Guenther and W. F. Walker, "Generalized cystic resolution: A metric for assessing the fundamental limits on beamformer performance," *IEEE Trans. Ultrason., Ferroelectr., Freq. Control*, vol. 56, no. 1, pp. 77–90, Jan. 2009.

[7] J. Ng, R. Prager, N. Kingsbury, G. Treece, and A. Gee, "Modeling ultrasound imaging as a linear, shift-variant system," *IEEE Trans. Ultrason., Ferroelectr., Freq. Control*, vol. 53, no. 3, pp. 549–563, Mar. 2006.

[8] O. Michailovich and A. Tannenbaum, "Blind deconvolution of medical ultrasound images: A parametric inverse filtering approach," *IEEE Trans. Image Process.*, vol. 16, no. 12, pp. 3005–3019, Dec. 2007.

[9] C. Yu, C. Zhang, and L. Xie, "A blind deconvolution approach to ultrasound imaging," *IEEE Trans. Ultrason., Ferroelectr., Freq. Control*, vol. 59, no. 2, pp. 271–280, Feb. 2012.

[10] G. F. Pinton, G. E. Trahey, and J. J. Dahl, "Erratum: Sources of image degradation in fundamental and harmonic ultrasound imaging: A non-linear, full-wave, simulation study," *IEEE Trans. Ultrason., Ferroelectr., Freq. Control*, vol. 58, no. 6, pp. 1272–1283, Jun. 2011.

[11] R. Y. Chiao and X. Hao, "Coded excitation for diagnostic ultrasound: A system developer's perspective," *IEEE Trans. Ultrason., Ferroelectr., Freq. Control*, vol. 52, no. 2, pp. 160–170, Feb. 2005.

[12] K. Ranganathan and W. F. Walker, "A novel beamformer design method for medical ultrasound. Part I: Theory," *IEEE Trans. Ultrason., Ferroelectr., Freq. Control*, vol. 50, no. 1, pp. 15–24, Jan. 2003.

[13] J. A. Jensen, "Field: A program for simulating ultrasound systems," *Med. Biol. Eng. Comput.*, vol. 4, no. 1, pp. 351–353, 1996.

[14] J. A. Jensen, "A model for the propagation and scattering of ultrasound in tissue," *J. Acoust. Soc. Amer.*, vol. 89, no. 1, pp. 182–190, 1991.

[15] J. W. Goodman, *Introduction to Fourier Optics*. Greenwood Village, CO, USA: Roberts & Company, 2005.

[16] S. Salles, H. Liebgott, D. Garcia, and D. Vray, "Full 3-D transverse oscillations: A method for tissue motion estimation," *IEEE Trans. Ultrason., Ferroelectr., Freq. Control*, vol. 62, no. 8, pp. 1473–1485, Aug. 2015.

[17] T. Stepinski, "An implementation of synthetic aperture focusing technique in frequency domain," *IEEE Trans. Ultrason., Ferroelectr., Freq. Control*, vol. 54, no. 7, pp. 1399–1408, Jul. 2007.

[18] A. J. Hunter, B. W. Drinkwater, and P. D. Wilcox, "The wavenumber algorithm for full-matrix imaging using an ultrasonic array," *IEEE Trans. Ultrason., Ferroelectr., Freq. Control*, vol. 55, no. 11, pp. 2450–2462, Nov. 2008.

[19] P. Kruizinga, F. Mastik, N. D. Jong, A. F. W. van der Steen, and G. V. Soest, "Plane-wave ultrasound beamforming using a nonuniform fast Fourier transform," *IEEE Trans. Ultrason., Ferroelectr., Freq. Control*, vol. 59, no. 12, pp. 2684–2691, Dec. 2012.

[20] C. Chen, G. A. G. M. Hendriks, R. J. G. V. Sloun, H. H. G. Hansen, and C. L. D. Korte, "Improved plane-wave ultrasound beamforming by incorporating angular weighting and coherent compounding in Fourier domain," *IEEE Trans. Ultrason., Ferroelectr., Freq. Control*, vol. 65, no. 5, pp. 749–765, May 2018.

[21] D. Liu, "Plane wave scanning reception and receiver," U.S. Patent 6 685 641, Feb. 3, 2004.

[22] J. Cheng and J.-Y. Lu, "Extended high-frame rate imaging method with limited-diffraction beams," *IEEE Trans. Ultrason., Ferroelectr., Freq. Control*, vol. 53, no. 5, pp. 880–899, May 2006.

[23] D. Garcia, L. Le Tarnec, S. Muth, E. Montagnon, J. Porée, and G. Cloutier, "Stolt's f-k migration for plane wave ultrasound imaging," *IEEE Trans. Ultrason., Ferroelectr., Freq. Control*, vol. 60, no. 9, pp. 1853–1867, Sep. 2013.

[24] J.-Y. Lu, "2D and 3D high frame rate imaging with limited diffraction beams," *IEEE Trans. Ultrason., Ferroelectr., Freq. Control*, vol. 44, no. 4, pp. 839–856, Jul. 1997.

[25] J.-Y. Lu, "Experimental study of high frame rate imaging with limited diffraction beams," *IEEE Trans. Ultrason., Ferroelectr., Freq. Control*, vol. 45, no. 1, pp. 84–97, Jan. 1998.

[26] A. G. J. Besson *et al.*, "A sparse reconstruction framework for Fourier-based plane-wave imaging," *IEEE Trans. Ultrason., Ferroelectr., Freq. Control*, vol. 63, no. 12, pp. 2092–2106, Dec. 2016.

[27] G. Alberti, H. Ammari, F. Romero, and T. Wintz, "Mathematical analysis of ultrafast ultrasound imaging," *SIAM J. Appl. Math.*, vol. 77, no. 1, pp. 1–25, Jan. 2017.

[28] L. Roquette, S. Matthieu, P. Hurley, and A. Besson, "On an analytical, spatially-varying, point-spread-function," in *Proc. IEEE Int. Ultrason. Symp. (IUS)*, Sep. 2017, pp. 1–4.

[29] D. G. Wildes, R. Y. Chiao, C. M. W. Daft, K. W. Rigby, L. S. Smith, and K. E. Thomenius, "Elevation performance of 1.25D and 1.5D transducer arrays," *IEEE Trans. Ultrason., Ferroelectr., Freq. Control*, vol. 44, no. 5, pp. 1027–1037, Sep. 1997.

[30] J. Jensen, "Ultrasound imaging and its modeling," in *Imaging Complex Media With Acoustic Seismic*. New York, NY, USA: Springer, 2000, pp. 1–38.

[31] S.-C. Wooh and Y. Shi, "Three-dimensional beam directivity of phase-steered ultrasound," *J. Acoust. Soc. Amer.*, vol. 105, no. 6, pp. 3275–3282, Jun. 1999.

[32] C. M. Bender and S. A. Orszag, *Advanced Mathematical Methods for Scientists and Engineers I: Asymptotic Methods and Perturbation Theory*. Springer, 2013.

[33] J. P. McClure and R. Wong, "Justification of the stationary phase approximation in time-domain asymptotics," *Proc. Roy. Soc. London. A, Math., Phys. Eng. Sci.*, vol. 453, no. 1960, pp. 1019–1031, May 1997.

[34] F. W. J. Olver, "Error bounds for stationary phase approximations," *SIAM J. Math. Anal.*, vol. 5, no. 1, pp. 19–29, 1974.

[35] D. A. Guenther and W. F. Walker, "Optimal apodization design for medical ultrasound using constrained least squares part I: Theory," *IEEE Trans. Ultrason., Ferroelectr., Freq. Control*, vol. 54, no. 2, pp. 332–342, Feb. 2007.

[36] Field-ii.dk. (2018). *Field II Ultrasound Simulation Program*. Accessed: Jun. 12, 2018. [Online]. Available: https://www.field-ii.dk/

[37] S. Salles, A. J. Y. Chee, D. Garcia, A. C. H. Yu, D. Vray, and H. Liebgott, "2-D arterial wall motion imaging using ultrafast ultrasound and transverse oscillations," *IEEE Trans. Ultrason., Ferroelectr., Freq. Control*, vol. 62, no. 6, pp. 1047–1058, Jun. 2015.

Chuan Chen (S'16) was born in Jiujiang, China, in 1992. He received the B.Sc. degree from the Huazhong University of Science and Technology, Wuhan, China, in 2013, and the M.Sc. degree in electrical engineering from the Eindhoven University of Technology, Eindhoven, The Netherlands, in 2016. He is currently pursuing the Ph.D. degree in ultrafast 3-D elastography for tumor detection in breast with the Medical UltraSound Imaging Center (MUSIC), Radboud University Medical Center, Nijmegen, The Netherlands.

Hendrik (Rik) H. G. Hansen (S'11–M'13) received the M.Sc. degree in applied physics from the Eindhoven University of Technology, Eindhoven, The Netherlands, in 2005, and the Ph.D. degree in noninvasive vascular ultrasound elastography, medical sciences, and radiology from the Radboud University Medical Center (Radboudumc), Nijmegen, The Netherlands, in 2012.

Since 2017, he has been a Work Group Leader in functional ultrasound imaging with the Medical UltraSound Imaging Center (MUSIC), Radboudumc.

Gijs A. G. M. Hendriks (S'15) received the M.Sc. degree in biomedical engineering from the Eindhoven University of Technology, Eindhoven, The Netherlands, in 2014, and the Ph.D. degree in 3-D breast ultrasound elastography, medical sciences, radiology, and nuclear medicine with the Radboud University Medical Center (Radboudumc), Nijmegen, The Netherlands, in 2019.

He has been holding a postdoctoral position in 3-D breast ultrasound elastography at the Medical UltraSound Imaging Center (MUSIC), Radboudumc, since July 2018.

Jan Menssen received the B.Sc. degree in electrical engineering from Polytechnical Institute, Breda, The Netherlands, in 1984.

Since 2005, he has been a Senior Research Engineer with the Medical UltraSound Imaging Center (MUSIC), Radboud University Medical Center, Nijmegen, The Netherlands.

Jian-Yu Lu (S'86–M'88–SM'99–F'08) received the B.Sc. degree in electrical engineering from Fudan University, Shanghai, China, in 1982, the M.Sc. degree in acoustics from Tongji University, Shanghai, in 1985, and the Ph.D. degree in biomedical engineering from Southeast University, Nanjing, China, in 1988.

Since 1997, he has been a Professor with the Department of Bioengineering, The University of Toledo (UT), Toledo, OH, USA, where he has been an Adjunct Professor with the College of Medicine and Life Sciences since 1998.

Chris L. de Korte (M'00–SM'15) received the M.Sc. degree in electrical engineering from the Eindhoven University of Technology, Eindhoven, The Netherlands, in 1993, and the Ph.D. degree in intravascular ultrasound elastography and medical sciences from Thoraxcenter, Erasmus University Rotterdam, Rotterdam, The Netherlands, in 1999.

Since 2004, he has been the Head of the Medical UltraSound Imaging Center (MUSIC), Department of Radiology and Nuclear Medicine, Radboud University Medical Center, Nijmegen, The Netherlands, where he has been a Medical Physicist since 2007 and a Full Professor of medical ultrasound techniques since 2015.